

Comparison of Different Figure of Merit Functions for Dynamic Single Photon Emission Computed Tomography (dSPECT)

Christophe Blondel¹, Dominikus Noll², Jean Maeght³, Anna Cellier⁴, *Member, IEEE*, Troy Farncombe⁵

¹ INRIA -ChIR, 2004 route des Lucioles, 06902 Sophia-Antipolis, France

² Université Paul Sabatier, Mathématiques pour l'Industrie et la Physique, 118 route de Narbonne, 31062 Toulouse, France

³ Artelys S.A., 215, rue Jean-Jacques Rousseau, 92136 Issy-les-Moulineaux, France

⁴ Vancouver Hospital & Health Sciences Center, Vancouver, BC, Canada V5Z 1M9

⁵ University of Massachusetts Medical School, Dep. of Nuclear Medicine, 55 Lake Ave. North, Worcester, MA 01655

Abstract

Dynamic Single Photon Emission Computed Tomography (dSPECT) is a technique which visualizes changing activity distributions in the human body, using dynamic emission data acquired during a single rotation of a standard SPECT camera system. The reconstruction process in dSPECT is based on nonlinear regularization and optimization techniques, and we presently compare a number of possible problem oriented figures of merit based on different spatial and temporal regularization techniques. The accuracy of dSPECT in terms of temporal and spatial resolution is tested in a simulated dynamic cardiac study and a dynamic renal patient study.

I. INTRODUCTION

Dynamic functional imaging with SPECT camera systems has been recognized as a promising new option for medical diagnostics, and several approaches to visualizing and quantifying dynamic parameters of time-varying processes in the body have recently been proposed (see [1, 2, 3, 4, 5, 6]). Dynamic Single Photon Emission Computed Tomography (dSPECT) is one such modality, whose most important aspect is its ability to reconstruct time-varying activity distributions from dynamic data acquired on a standard protocol with a single rotation of the camera system (cf. [10]). Image reconstruction in dSPECT is based on nonlinear regularization and optimization techniques (cf. [7, 8]), but dynamic versions of the EM-algorithm have also been found and tested (see [5, 9]). The way dSPECT deals with the problem of inconsistent projections was validated in a number of studies, including simulations, phantom and patient experiments.

It should be emphasized that casting dynamic SPECT as an ill-posed inverse problem points to several solution strategies via regularizing techniques, but does not stipulate a unique possible figure of merit. We therefore compare a Poisson and a Gaussian objective, both to be employed in tandem with suitable problem oriented regularizers. We validate our choices using a simulated dynamic cardiac study and a dynamic renal patient study.

The choice of the acquisition protocol may have a strong

influence on the performance of the dSPECT method. Optimal acquisition protocols in clinically relevant situations have recently been proposed in [10].

II. METHODS

Image reconstruction in dSPECT is no longer based on filtered backprojection or the well-known iterative methods. Instead, a large scale nonlinear optimization problem of the form

$$(P) \quad \begin{array}{ll} \text{minimize} & \mathcal{F}(f, Rf - d) \\ \text{subject to} & f_{i1} \leq f_{i2} \leq \dots \leq f_{ip_i} \\ & f_{ip_i} \geq f_{ip_{i+1}} \geq \dots \geq f_{iS} \\ & f_{ik} \geq 0 \end{array}$$

is solved. Here $\mathcal{F}(f, e)$ is an appropriate figure of merit function which attributes a cost to a possible dynamic image f , R is the attenuated dynamic Radon transform, and $e = Rf - d$ is the forward error between the observed data d and the hypothetical projection data Rf . The constraints in (P) are referred to as *shape constraints*, since they determine the overall profile or shape of the pixel curves. The case above is when every single dixel (dynamic pixel) i has increasing activity during the initial times k of the scan, $0 \leq k \leq p_i$, reaches its peak activity at time $k = p_i$, and decays during the remaining times $p_i \leq k \leq S$, (S is the number of stops or times). The peak time p_i for the activity curve in pixel i may vary from pixel to pixel.

We mention a different type of shape constraints using second order information. For instance, we may assume the time profile in the i th pixel to be concave between times $k = 0$ and $k = q_i$, q_i the inflection point, and convex during the remaining times $k = q_i, \dots, S$, a shape often encountered in applications, and built into constraints through second differences. Setting $f'_k = f_k - f_{k-1}$, $f''_k = f'_k - f'_{k-1}$, we let

$$f''_1 \geq 0, \dots, f''_{q_i-1} \geq 0, \text{ and } f''_{q_i+1} \leq 0, \dots, f''_{S-2} \leq 0$$

to be used along with positivity constraints, $f_{ik} \geq 0$.

Returning to (P) above, the peak positions p_i for the pixels i are determined automatically by an extra optimization step, performed prior to the actual image reconstruction (P) . The present paper will also contribute a new method of peak

detection, which has several new features compared to the method [8] we previously applied. In particular, the new approach gives a rapid estimation of the shape of the expected time profiles, and is used to establish good initial estimates for the main optimization routine, an important aspect, as we are facing large scale optimization problems.

A first figure of merit function tested in a number of situations includes the negative log-likelihood of a weighted Gaussian law

$$\mathcal{F}_1(f, Rf - d) = \frac{1}{2} \|\Sigma^{-1/2}(Rf - d)\|^2 + \mathcal{S}(f), \quad (1)$$

where $\mathcal{S}(f)$ is a properly chosen regularizing or smoothing term derived e.g. from a prior Bayesian model of the space of dynamic images f . Typical examples will be presented and discussed in the next section.

An alternative figure of merit is obtained if the emission data d are modelled by a Poisson statistic. Then the cost should be

$$\mathcal{F}_2(f, Rf - d) = \sum_{j,k} \left(\sum_i R_{ijk} f_{ik} - d_{jk} \log \left(\sum_i R_{ijk} f_{ik} \right) \right) + \mathcal{S}(f) \quad (2)$$

where i is summation over pixels (voxels), j over bins, and k over angular positions (stops). The left-hand term in \mathcal{F}_2 is, up to constants, the negative log-likelihood of the Poisson law, while \mathcal{S} is a smoothing term arising from a Bayesian approach as before.

A forerunner of dSPECT, first published in [11], assumed a two-compartment model of the underlying tracer dynamics of a Tc99m-based fatty acid heart study. Here the nonlinear optimization model was

$$\begin{aligned} & \text{minimize} && \mathcal{F}(f, Rf - d) \\ (NLS) & \text{subject to} && f_{ik} = A_{i1}e^{-\lambda_{i1}k} + A_{i2}e^{-\lambda_{i2}k} + A_{i3} \\ & && \lambda_{i1} \geq \lambda_{i2} \geq 0 \\ & && A_{i1} + A_{i2} + A_{i3} \geq 0 \end{aligned}$$

where the figure of merit could be chosen as above. It was shown in [6, 12] that this model is numerically difficult, and in many cases performs weaker than (P), even when the hypothesis of an underlying two-compartment model is correct. Notice that subject to some important modifications, (NLS) has recently been revived in a number of approaches (cf. [2, 3]). In these approaches, the major differences from [11] are in particular the choice of the spatial basis functions, the model of the blood input function, and the fact that pixels i , prior to reconstruction, were divided into a static and a dynamic part in order to reduce the number of unknown parameters $A_{i\nu}$ and $\lambda_{i\nu}$ to be fitted.

III. SPATIAL AND DYNAMIC REGULARIZERS

The need to enhance image reconstruction methods by regularization techniques is widely recognized (cf. for instance [13]). It applies to static SPECT or PET image processing

just as to other reconstruction techniques originating from mathematically ill-posed problems. This points to a major drawback of most iterative techniques, like the EM-algorithm (and its variations), since they are basically in conflict with the need of spatial regularization. Namely, these methods hinge on the possibility to process pixels *separately* in the M-step (and its counterparts), while spatial regularization requires just the opposite, that is, *mixing* pixels when applying local filters. In our opinion, this is a strong point for using optimization techniques, even though some ideas to include spatial filtering into EM-like iterations do exist (see e.g. [9]).

In dSPECT, we find it useful to insist on two types of regularization, spatial filtering, as already apparent in static SPECT or PET, and dynamic filtering applied to the time series in each dynamic pixel. We shall subsequently comment on some of the regularizers used in dSPECT reconstructions. For spatial regularizers, a rich literature in the domain of image processing is of course available. We refer to [13] for a presentation from an ECT point of view. On the other hand, dynamic filtering is a new issue in ECT, and successful figures will have to be established empirically.

A spatial filter useful to SPECT and dSPECT based on ideas from [14] is

$$\mathcal{S}(f) = \frac{\alpha}{2} \|\mathcal{H}_b f\|_2^2 = \frac{\alpha}{2} \|\phi_b \cdot \hat{f}\|_2^2. \quad (3)$$

Here $\mathcal{H}_b f$ is a spatial high pass filter with cutoff frequency b . The second equality indicates that this regularizer may be conveniently implemented via 2D FFT and using Parseval's identity: choose a 2D lag window function $\phi_b(s)$ having $\phi_b(0) = 0$ and $\phi_b(s) = 1$ for $|s| \geq b$.

The rationale of (3) is in the Fourier slice theorem: $F_1[Rf(\cdot, \theta)](\sigma) = \hat{f}(\sigma\theta)$, (cf. [16], where $F_1[\cdot]$ is the 1D Fourier transform with respect to the s -variable). It tells us that in the absence of tissue attenuation, any detail apparent in the image f should also be visible in some of the projections $Rf(\cdot, \theta)$. Or put differently, any detail *smaller* than $2\pi/b$ in a candidate image f , (b is the known spatial bandwidth of the sinogram), should be attributed to a noise source, as it could not originate from the data. Following the idea of regularization, we do not simply suppress high frequencies in the reconstructed images. Instead, a high cost (3) is attributed to these high frequencies, and the optimizer will therefore try to avoid them.

Naturally, in cases where attenuation may not be ignored, the Fourier slice theorem is only approximately correct, and some of the details of f will be smoothed away in Rf due to tissue attenuation and scatter. We then have to be conservative when choosing the cutoff bandwidth b , which should be mildly above the known bandwidth of the sinogram. For all that, this filter works well in practice, and we strongly recommend its use here.

A variant to (3) is

$$\mathcal{S}(f) = \frac{\alpha}{2} \|\mathcal{H}_b(Rf)\|_2^2 = \frac{\alpha}{2} \|\psi_b \cdot F_1[Rf]\|_2^2, \quad (4)$$

where \mathcal{H}_b is now a 1D spatial high pass filter applied to the spatial spectrum of the sinogram. Here ψ_b is the corresponding 1D cutoff function, $\psi_b(0) = 0$, $\psi_b(s) = 1$ for $|s| \geq b$. Even though mathematically equivalent to (3) in the un-attenuated case, the two regularizers behave slightly different in practice (see [12] for more details).

It was shown in [15] that the 2D spectrum of the dynamic attenuated Radon transform, $\widehat{R}f$, is concentrated on a region of bowtie shape as shown in Figure 1. This fact was previously known (cf. [17, 16]) in the static case. Using a 2D cutoff function $\phi_{b,m}$ adapted to the bowtie shape, we are led to consider a regularizing term of the form

$$\mathcal{S}(f) = \frac{\alpha}{2} \|\phi_{b,m} \cdot \widehat{R}f\|_2^2. \quad (5)$$

Here $\phi_{b,m}(0) = 0$ and $\phi_{b,m}(s) = 1$ for s outside a bowtie of vertical thickness $2m$ at $(0,0)$ and of horizontal width $2b$, where b is again the spatial bandwidth of the sinogram (see [15] for details).

A numerical experiment to compare the spatial regularizers (3) and (5) is presented in Table 1 below. We consider the figure of merit

$$\frac{1}{2} \|Rf - d\|_2^2 + \frac{\alpha_1}{2} \|\phi_{m,b} \cdot \widehat{R}f\|_2^2 + \frac{\alpha_2}{2} \|\phi_b \cdot \hat{f}\|_2^2, \quad (6)$$

where R was chosen as the classical static Radon transform, discretized over 180° using 64 stops and 64 camera bins for a 64×64 image grid. Notice that the Hessian of (6) is

$$R^T R + \alpha_1 R^T \overbrace{F_2^T \Phi_{b,m}^2 F_2}^{H_1} R + \alpha_2 \overbrace{F_2^T \Phi_b^2 F_2}^{H_2}$$

Here $\Phi_{b,m}$ is a matrix representing the cutoff function $\phi_{b,m}$ of bowtie shape in the sinogram space, Φ_b is the matrix for the 2D cutoff ϕ_b in image space, and F_2 is the 2D FFT.

Hessian	λ_{\max}	λ_{\min}
$R^T R$	3918	0
$R^T H_1 R$	276	0
H_2	1	0
$R^T R + \alpha_1 R^T H_1 R$	*	0
$R^T R + H_2$	3918	0.4
$R^T R + 10^3 H_2$	3918	2.0
$R^T R + 10^4 H_2$	10099	2.1
$R^T R$ projected	3917	2.2
$R^T R + R^T H_1 R + 10^3 H_2$	3919	3.5
$R^T R + 10 R^T H_1 R + 10^3 H_2$	3928	9.1
$R^T R + 10^2 R^T H_1 R + 10^3 H_2$	27795	27

Table 1

Extremal eigenvalues of regularized objective

The interpretation of Table 1 is as follows. Line 1 shows that the Radon transform, even though theoretically injective, is rank deficient in practice due to the symmetries in the

geometry. Lines 2 and 3 give the extremal eigenvalues of the regularizers in case $\alpha_1 = \alpha_2 = 1$. Line 4 shows that regularizer (5) barely improves the condition number if used without regularizer (3). Lines 5 to 7 show that regularizer (3) makes the Hessian invertible. The value $\alpha_2 = 10^3$ seems optimal here. Lines 9 - 11 show that the regularizer (5), if used in tandem with (3), improves the condition number of the Hessian $R^T R + 10^3 H_2$.

As introduced and used in our experiments, the spectral filters(3), (4) and (5) use the Euclidean norm, which is certainly *the* natural candidate. Notice however that in the case of Tychonov regularization, $\mathcal{S}(f) = \frac{\alpha}{2} \|f\|_2^2$, the 2-norm does often have too strong a smoothing effect. As a remedy, the following 1-norm term

$$\mathcal{S}(f) = \frac{\alpha}{2} \|\nabla_x f\|_1 \quad (7)$$

has been proposed. It has been verified experimentally that (7) tends to privilege flat zones in reconstructed images. It may therefore be envisaged to use the 1-norm for the spectral filters as well. Notice that in each case, the implementation of the spatial gradient $\nabla_x f$ uses finite difference approximations of the partial derivatives. In the case of (7), we have used the usual scheme shown in Figure 2.

Temporal filters are needed in dSPECT reconstructions, and may be based on the same philosophy: use whatever type of prior information available to avoid unrealistic reconstructions f , bearing in mind that in an ill-posed problem many unrealistic candidates f will match the available data within an acceptable tolerance in the sense that they saturate the noise level: $\|Rf - d\|^2 \approx \text{Var}(d)$ (see Section IV). Here we shall limit ourselves to two examples, leaving the more straightforward adoptions of the above spatial filters to the reader.

Our first example is motivated by a dynamic physical phantom [19] built at the Vancouver Hospital. The phantom heart consists of several small cylindrical containers with a drain and an inflow. Each container is equipped with a mixing propeller to guarantee a homogeneous flow. Tuning the motor which steers the pump may, in principle, produce arbitrary activity profiles in the containers. Consider the situation of washout, where the container is initially filled with activity $f(0)$. Pumping fresh water at flow rate $R(t)$ means that the remaining activity in the container of volume V at time t is

$$f(t) = f(0) \exp \left\{ - \int_0^t \frac{R(\tau)}{V} d\tau \right\}.$$

The idea is now to avoid highly irregular curves $f(t)$ by penalizing irregular behavior of the motor. In a sense, the most natural profile is flow with constant rate, $R'(t) = 0$. In terms of f , this leads to $R'/V = -(f'/f)' = -(\log f)'' = 0$. In the continuous model, the dynamic regularizer could therefore be chosen as

$$\mathcal{S}(f) = \frac{\alpha}{2} \int_0^T \left((\log f(t))'' \right)^2 dt, \quad (8)$$

T the total time of the scan. Discretizing into time steps $k = 1, \dots, S$ via finite differences leads to the regularizer

$$\mathcal{S}(f) = \frac{\alpha}{2} \sum_{i=1}^N \sum_{k=2}^S \left(\log f_{i,k+1} + \log f_{i,k-1} - 2 \log f_{i,k} \right)^2. \quad (9)$$

The rationale of (8), (9) is that if every cell acts similar to the macroscopic containers of the phantom heart, the optimizer (P) will privilege uniform flow, and this will have the desired smoothing effect.

As a second example one may use the dynamic analogue of the spatial Fourier high pass filter (3). As already observed in [15], this requires an additional step if applied to decreasing-only profiles, which are discontinuous signals in the space of periodic functions. Fourier filters, if applied directly to these curves, would bear the risk of blurring the signal at the initial times, due to the inherent discontinuity. To overcome this problem, [15] proposes to flip the discontinuous signal, and to apply a 1D Fourier filter to the doubled, and therefore continuous, time curves. The ideas are detailed in that reference.

IV. NOISE LEVEL AND STOPPING

A practical question related to the use of *any* of these regularizers is the correct choice of the penalty constant α . A good rule of thumb is to use α to steer the mean square error $\|Rf - d\|_2^2$ towards its expected value $\sum_{jk} \text{Var}(d_{jk}) \approx \sum_{jk} d_{jk}$, where the latter assumes a Poisson statistic for the emission data. This works well in practice, and the correct value α for a given setting is easily found.

V. PEAK DETECTION

Since we are interested in studies representing wash-in *and* washout periods of a dynamic tracer, the use of the shape constrained model (P) requires, prior to reconstruction, locating the peak position p_i in each individual pixel i . In some cases, a rough estimate of the peak time may be obtained by inspecting the projection data, but this is not always a reliable indicator, in particular when attenuation is sizable and tends to affect the shape of the profiles. Here we propose a method of peak detection, which in our testing proved extremely fast and efficient. Using a variant of model (P), we fit to each activity curve in each pixel i a hat-shaped curve as displayed in Figure 3 (left), using four unknown parameters, x_{i1} = left-end activity, x_{i2} = peak position, x_{i3} = peak height, and x_{i4} = right-end activity. Writing $f_{ik} = h_k(x_i)$, where $x_i = (x_{i1}, \dots, x_{i4})$, and where h_k samples the continuous hat function at time k , we solve the optimization problem

$$\begin{aligned} (\Lambda) \quad & \text{minimize} \quad \frac{1}{2} \|Rh(x) - d\|^2 + \mathcal{S}(h(x)) \\ & \text{subject to} \quad x_{i1} \geq 0, x_{i3} \geq x_{i1}, x_{i3} \geq x_{i4} \geq 0 \end{aligned}$$

for the decision variable $x = (x_i)$. Here $\mathcal{S}(f) = \mathcal{S}(h(x))$ is a spatially regularizing term as used before. Solving (Λ) serves

four different purposes. Along with the peak position, we get an estimation of the peak activity, and we may choose the hat-shaped dynamic image $f = h(x)$ as a first indicator for the overall dynamics in the image. Finally, we may use the hat shaped functions as indicators whether a pixel is really dynamic.

A natural extension of the hat-shape is the extended hat shown in Figure 3 (right), featuring eight determining parameters. In addition to the properties of the simple hat, the extended hat has the advantage that it may be used to generate good initial guesses for the dynamic profiles expected in the final dSPECT reconstruction process (P).

VI. DETECTING DYNAMIC PIXELS

In many cases, the truly dynamic region is only a small part of the image, and it is possible to identify pixels whose activity will be merely static. This will reduce the number of unknown parameters in the final reconstruction procedure (P). We subsequently outline one way in which the reconstruction based on hat-shaped functions (Figure 3, left) may be used to decide whether the activity in pixel i should be held constant or considered dynamic. We propose the following steps:

Firstly, for every pixel i , we determine the amplitude $\Delta_i = \max_k f_{ik} - \min_k f_{ik}$ of the reconstructed curve in pixel i . We arrange amplitudes in decreasing order, $\Delta_{i_1} \geq \Delta_{i_2} \geq \dots \geq \Delta_{i_N}$, where N is the total number of pixels. Secondly, we require an (over)estimation of the percentage δ of dynamic pixels in the image. In a cardiac study, this should be easily obtained by drawing a zone around the heart using a preliminary reconstruction (obtained e.g. via static EM). We then consider the first $\delta \cdot N$ among pixels i_1, i_2, \dots as dynamic, fixing the remaining as static. Clearly, as a by-product, the reconstruction using hat functions also finds the pixels outside the contour, since the reconstruction returns flat hats at value 0. Notice that the outlined method could be applied to *any* type of reconstruction not necessarily based on hat functions. The reason why we apply it to hat functions is the superior speed of model (Λ).

If an estimation of δ is difficult to obtain, e.g. in a brain study, where almost every pixel might be dynamic, we may still choose a threshold to decide which pixels should be kept as dynamic. In the worst case, this may be the entire contour.

VII. COMPARTMENTAL MODELLING

It is well-known from PET and planar scintigraphic imaging that quantitative information about dynamics may be obtained by drawing regions of interest and fitting exponential models to the extracted curves. The driving idea behind the nonlinear least squares model (NLS) was to adopt compartmental modelling directly into the SPECT reconstruction process (cf. [11], see also [2, 3]). While this is an appealing idea, it becomes clear rather quickly that the instability inherent to fitting exponential models, well-known even in cases where the curves are already *given*, (cf. [18]), will be even more disastrous when we have to

reconstruct these curves.

This numerical problem, in tandem with the more obvious criticism that compartmental models are merely heuristic or even purely descriptive approaches, made us dispense with compartmental models in the dSPECT image reconstruction (P). As we shall see, there is a more subtle way to use prior information included in a compartmental model of the tracer dynamics, by incorporating it in a special dynamic regularizer. We subsequently describe this approach in the case of a two compartment model. It will become clear in which way the idea would have to be changed when applied to models with more compartments.

Assuming a localized two compartment dynamic with constant input function, the expected discretized dynamic profiles are of the form

$$f_{ik} = f_i(t_k) = A_{i1}e^{-\lambda_{i1}k} + A_{i2}e^{-\lambda_{i2}k} + A_{i3} \quad (10)$$

with parameters $\lambda_{i1} \geq \lambda_{i2} \geq 0$ and $A_{i3} \geq 0$, $A_{i1} + A_{i2} + A_{i3} \geq 0$. In practice there are two cases of major interest, profiles with decreasing activity, and the more complicated case of increasing-decreasing activities.

In order to circumvent the numerical difficulties of the exponential models, we observe that every bi-exponential curve f_{ik} satisfies a difference equation of the form

$$f_{ik} = a_{i1}f_{i,k-2} + a_{i2}f_{i,k-1} + a_{i3}, \quad (11)$$

where the five parameters $A_{i1}, A_{i2}, A_{i3}, \lambda_{i1}, \lambda_{i2}$ per pixel in (10) correspond to the five pieces of information a_{i1}, a_{i2}, a_{i3} and f_{i1}, f_{i2} in (11). Clearly (11) also contains oscillatory solutions which are not of the form (10), but in the context of shape constraints in (P), oscillatory profiles f are not feasible. It is therefore reasonable to use a regularizer of the form

$$S(f; a) = \frac{\alpha}{2} \sum_{i,k} (f_{ik} - a_{i1}f_{i,k-2} + a_{i2}f_{i,k-1} + a_{i3})^2. \quad (12)$$

Remark. Notice that fitting a model (10) to a given curve f_{i1}, \dots, f_{iS} via the equivalent form (11) is known as Prony's method. In its traditional form, one may ignore the implicit constraints, which force non-oscillatory solutions, because experience shows that even oscillatory curves will generally follow the overall shape of the given data. In contrast, in (P), Rf and not f is sampled, so Prony's approach is used to reconstruct the curves f , and is therefore significantly less stable. Avoiding oscillatory curves via shape constraints, as we do it, is then well-advised.

In order to implement this approach, the basic program (P) is extended to an optimization over the joint decision variable (f, a) :

$$\begin{aligned} & \text{minimize} && \mathcal{F}(f; Rf - d) + S(f; a) \\ & \text{subject to} && \text{shape constraints as in } (P) \\ (\tilde{P}) & && -1 \leq a_{i1} \leq 0, 0 \leq a_{i2} \leq 2, \\ & && a_{i2}^2 + 4a_{i1} \geq 0, a_{i1} + a_{i2} \leq 1, \\ & && a_{i1} + a_{i2} \geq 0, a_{i2} \geq 0 \end{aligned}$$

(\tilde{P}) is difficult to solve in practice if the number of dynamic pixels is large. A relaxation which works sufficiently well in applications is to regard the variables a as parameters, and to make a limited number of consecutive updates of a and α . This strategy has been used in our experiments.

If the influence of the bolus input function is still strongly felt during the initial time of the scan, the difference equation (11), which assumes a constant input function, is only gradually correct, and the regularizer $S(f; a)$ may have to be used with care. One obvious way to proceed is to use $S(f; a)$ only during the later times of the scan, where the influence of the fast dynamics stemming from the bolus have settled down, and the eigen dynamic of the compartmental system prevails. On the other hand, if prior information on the expected shape of the bolus function is available, this may be included into (11), resulting in a refined regularizing term $\mathcal{S}(f; a)$. We emphasize, however, that even in the case where (11), due to a strong bolus, is not entirely correct, the mere fact that we are using the compartmental model only as a regularizer and do not impose it by forcing the form (10), makes our approach highly flexible. The presented clinical study seems to confirm this.

VIII. PATIENT STUDY

A renal Tc-99m DTPA GFR on a normal patient was determined via dSPECT using a Siemens E-cam camera with two heads at 90° , each head rotating over 90° . Acquisition was started 2 minutes after injection, and the total time of the scan was 20 minutes. The reconstructed time profiles show a typical increasing decreasing shape with a peak activity after about 3 minutes. Comparison of the weighted least squares and Poisson model shows that the Poisson model produces smoother curves which resemble the accumulated curves obtained by a planar DTPA scan performed on the same test person prior to the dSPECT session. Performance of the two optimization methods is presented in Table 2.

Figure of Merit	Stopping Criterion	Number of Evaluations	Computation Time	$\ Rf - d\ _2$ $\ d\ _2$
\mathcal{F}_1	10^{-6}	680	31 minutes	21%
\mathcal{F}_2	10^{-6}	368	17 minutes	21%

Table 2

Performance of the two optimization methods for patient study

As outlined in Section I, the images are obtained using a complex procedure which starts with a static OS-EM reconstruction which despite the dynamic allows recognizing the overall shape. This reconstruction may already be used to determine the patient contour, and to estimate the percentage δ of dynamic versus static pixels. In a second step we obtain a reconstruction via hat functions. This determines the peak in each pixel, and provides two dynamic zones shown in Figure 4. The final step consists of running (P) with a limited number of dynamic pixels to obtain dynamic profiles of nearly bi-exponential shape, reflecting the approximately correct two

compartment model. Notice that the shape of the curves we expect is at least approximately known, since Tc99m-DTPA is used in planar imaging, and known to produce similar curves of bi-exponential shape.

IX. SIMULATED HEART STUDY

The simulation presented here is aimed at possible future clinical tests with Tc-99m Teboroxime or Thallium TI-201 in order to assess the sanguine perfusion rate of the myocardium. See [1] and the references given there for related canine studies. We assume a myocardium slice with two dynamic zones showing different time profiles. The chosen ideal activities correspond to a realistic dose of a scan of 12 minutes duration, starting immediately after injection. The ideal projection data were obtained using a realistic attenuation map, and were noised according to a Poisson statistics. The activities were adjusted to produce realistic projection data as observed in comparable clinical situations.

The goal of the simulation was to test the capability of dSPECT to reconstruct the different time profiles in the two zones of the myocardium, to test their accuracy, and in particular, to identify the cross-over of the two curves shown in line 2, Figure 8. As can be seen in Figure 8 right, dSPECT was in fact able to detect the cross-over of the curves from the two zones of the myocardium.

The simulation was based on a dynamic phantom image shown in Figure 6 line 1 at different times. The phantom heart was divided into two zones exhibiting different time behavior shown in Figure 8 left. The lungs spinal cord and background were given constant activities. A realistic attenuation map was used to generate ideal sinogram data shown in Figure 6, line 2 left. The study corresponded to a double head camera at 90 degrees angle, each head rotating over 90 degrees. The image resolution is 64×64 , a camera cross section has 64 bins in a line, and the camera took 64 stops on a time scale of 15 minutes. The tissue attenuation map was supposed known on the same 64×64 grid, and included in the operator R . The ideal sinogram was noised using Poisson statistics and assuming a realistic count rate in the projection data (Figure 6, line 2 right).

As a first step in the reconstruction process, the program (Λ) fitting hat functions was started and the result was used to detect peak times and to distinguish between static and dynamic pixels as outlined in Sections V and VI. The results for \mathcal{F}_1 and \mathcal{F}_2 are shown in Figure 7, line 1 left and middle. Due to strong attenuation, the region around the spinal cord was erroneously interpreted as dynamic.

Finally, program (P) with the two compartment regularizer $S(f; a)$ from Section VII was started based on the information provided by (Λ). In order to evaluate the dynamic information in the reconstruction, the curves for the two different zones of the heart were extracted and averaged to be tested against the true dynamic input (Figure 8 right versus Figure 8 left). The result shows that the peak positions as well as the overall shape of the curves were correctly represented, while the peak

activities were underestimated by approximately 8%.

X. CONCLUSION

In dSPECT, the problem of reconstructing changing activity distributions from dynamic and therefore inconsistent data, acquired by a slow rotating camera system, is addressed by an optimization approach, which uses spatial and temporal regularizers in order to add available prior information to the otherwise highly under-fitted system of equations.

Based on a patient study and a simulated case study, we compared dynamic SPECT reconstructions with a Gaussian and Poisson model for the emission data. Several dynamic and spatial regularizers were used in tandem with the data matching terms, leading to different figures of merit in our optimization approach (P). The tests show that both models are capable to reconstruct, within an acceptable error margin, the changing activities from dynamic emission data acquired with slowly rotating SPECT cameras. In the presented cases, the Poisson objective needed less CPU. The spatial regularizer which performed best was (3), but the flat zone regularizer (7) also produced interesting results. The dynamic regularizer we recommend for studies with increasing decreasing activities is (12), since it produced activity curves close to the bi-exponentials expected in regard of the prior information.

XI. REFERENCES

- [1] Khare HS, DiBella EVR, Kadrmas DJ, Christian PE, Gullberg GT, Comparison of static and dynamic cardiac perfusion Thallium-201 SPECT, *IEEE Trans. Nucl. Sci.* 48, no. 3, 2001, 774 – 779.
- [2] Maltz J, Pollak E, Budinger T: Multistart optimization algorithm for joint spatial and kinetic parameter estimation in dynamic ECT. *1998 IEEE Med. Imaging Conf. Rec.*, 1998.
- [3] Maltz JS: Optimal time-activity basis selection for experimental spectral analysis in dynamic emission tomography. *2000 IEEE Med. Imaging Conf. Record*, Lyon.
- [4] Reutter B, Gullberg G, Huesman R. Kinetic parameter estimation from attenuated SPECT projection measurements. *IEEE Trans. Nucl. Sci.* 45(6):3007 – 3013, 1998.
- [5] Bauschke HH, Noll D, Celler A, Borwein J: An EM-algorithm for dynamic SPECT tomography. *IEEE Trans. Med. Imaging* 18(3):252 – 261, 1999.
- [6] Farncombe T, Celler A, Noll D, Maeght J, Harrop R: Dynamic SPECT imaging using a single camera rotation (dSPECT). *IEEE Trans. Nucl. Sci.* 46(4):1055 – 1061, 1999.
- [7] Maeght J, Noll D, Boyd S: Dynamic emission tomography - regularization and inversion. *Canadian Math. Society, Conf. Proc.* Special issue on the occasion of J. Borwein's award of a Dhc, Limoges, France, 1999.
- [8] Farncombe T, Celler A, Bever C, Noll D, Maeght J, Harrop R: The incorporation of organ uptake into dynamic SPECT (dSPECT) image reconstruction. *IEEE Trans. Nucl. Sci.* to appear.
- [9] Farncombe T, Blinder S, Celler A, Noll D, Maeght J, Harrop R: A Dynamic Expectation Maximization Algorithm for Single

Camera Rotation Dynamic SPECT (dSPECT). *IEEE MIC Conference Record, Lyon 2000*.

- [10] Celler A, Farncombe T, Maecht J, Noll D, Harrop R: Optimization of acquisition and reconstruction protocols for dynamic single photon emission computed tomography (dSPECT). *Proc. of the 1999 Int. Meeting on Fully 3D Image Rec. in radiology and Nuclear Med.* 189 – 192, 1999.
- [11] Limber MN, Celler A, Barney JS, Limber MA, Borwein JM: Direct reconstruction of functional parameters for dynamic SPECT. *IEEE Trans. Nucl. Sci.* 42:1249 – 1256, 1995.
- [12] Maecht J: Analyse et méthodes pour un problème inverse en tomographie dynamique. *Thèse de Doctorat de l'Université Paul Sabatier, Toulouse, France 2000*.
- [13] Higdon DM, Bowsher JE, Johnson VE, Turkington TG, Gilland DR, Jaszczak RJ: Fully Bayesian estimation of Gibbs hyperparameters for emission computed tomography data, *IEEE TMI*, 16, 1997, 516 – 526.
- [14] Maréchal P, Togane D, Celler A: A new reconstruction methodology for computed tomography: FRECT (Fourier Regularized Computed Tomography). *1999 Conf. Rec. IEEE Med. Imag. Conf., Seattle*.
- [15] Maecht J, Noll D: Resolution in dynamic emission tomography. *SIAM J. Math. Analysis* 31, no. 5, 2000, pp. 1100 – 1120.
- [16] Natterer F, *The Mathematics of Computerized Tomography*, Teubner Verlag, Stuttgart, 1986.
- [17] Rattay PA, Lindgren AG: Sampling the 2-D Radon transform, *IEEE Trans. Acoustics, Speech, Signal Proc. ASSP-29*, 1981, 994 – 1002.
- [18] Kammler DW, Least squares approximation of completely monotonic functions by sums of exponentials, *SIAM J. Numer. Anal.* 16, 1979, 801 – 818.
- [19] Celler A, Farncombe T, Harrop R, Lyster D: Dynamic heart-in-thorax phantom for functional SPECT. *IEEE Trans. Nucl. Sci.* 44(4):1600 – 1605, 1997.

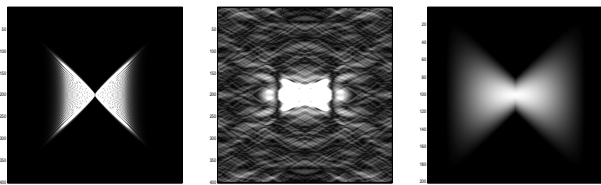


Fig. 1 Left hand picture shows the theoretical sinogram of a dynamic point source at $(.56, .8285)$ with dynamic profile $f(t) = e^{-\lambda(2\pi/T)t}$. Middle picture shows the bowtie obtained by an experiment with the dynamic heart-in-thorax phantom [19] with the same dynamic profile. Right hand picture shows a filter $\phi_{b,m}$ adapted to this dynamic scale.

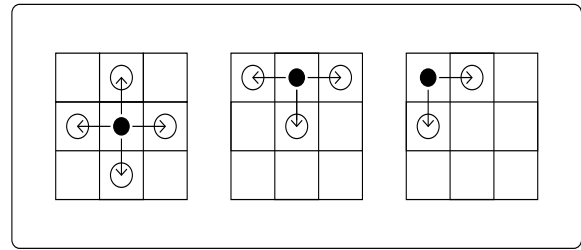


Fig. 2 Finite difference scheme for gradient approximation.

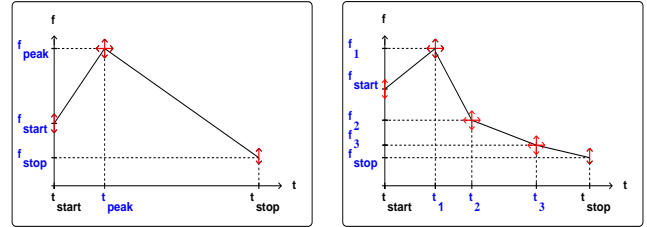


Fig. 3 Hat-shaped function (left) with 4 degrees of freedom, generalized hat (right) with 8 degrees of freedom.

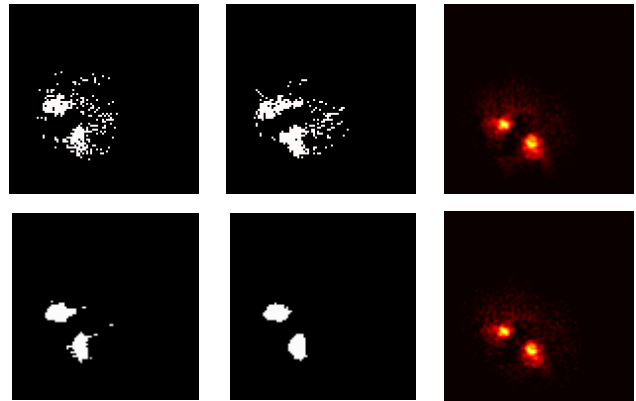


Fig. 4 Line 1 shows the result of fitting a hat function (left), a generalized hat function (middle), and identifying dynamic pixels with the method described in section in V. Line 2 shows result of 3×3 and 5×5 median filtering applied to the left hand image in line 1. Line 1 right shows the \mathcal{F}_1 reconstruction, line 2 right the \mathcal{F}_2 reconstruction.

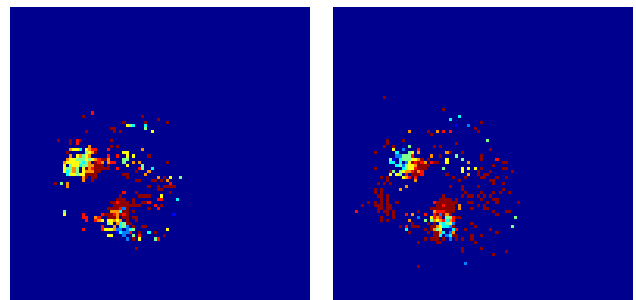


Fig. 5 Patient Study: Peak times as a color plot using \mathcal{F}_1 left-t and \mathcal{F}_2 right. Early peaks in blue, late peaks in red. The result shows that the peak activity occurs in the cortex first, and in the medula later.

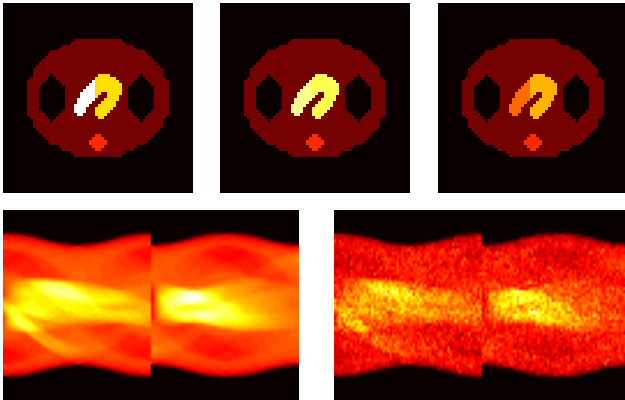


Fig. 6 Simulated Heart Study: Line 1 shows the dynamic phantom at times 10, 20 and 40. The heart is divided into two zones showing different dynamic profiles shown in Figure 7 line 1 (left). The lungs, spine and background have constant activities. Line 2 (left) shows the ideal sinogram, line 3 (right) the noised sinogram assuming a Poisson statistic and a realistic count rate. The data are created using a correctly scaled attenuation map

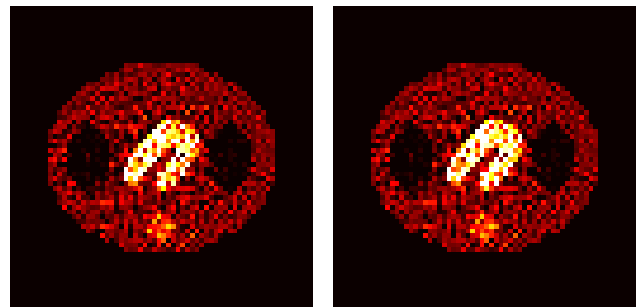
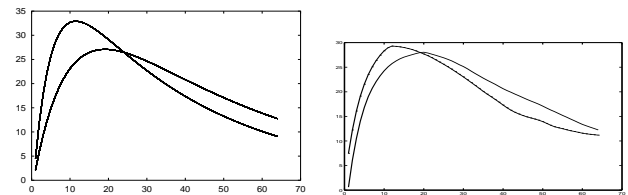


Fig. 8 Simulated Heart Study: Line 1 (left) shows the true dynamic curves assumed in the two parts of the heart (lesion versus healthy tissue). The curves on the right hand side are obtained by drawing the corresponding regions in the reconstructed heart (Poisson objective with approach (\hat{P})), and averaging the individual pixel curves. The peak positions and shapes are accurately represented. The peak activity for the faster dynamic is underestimated by roughly 10%. Line 2 shows the \mathcal{F}_2 reconstruction at times 10 and 20.

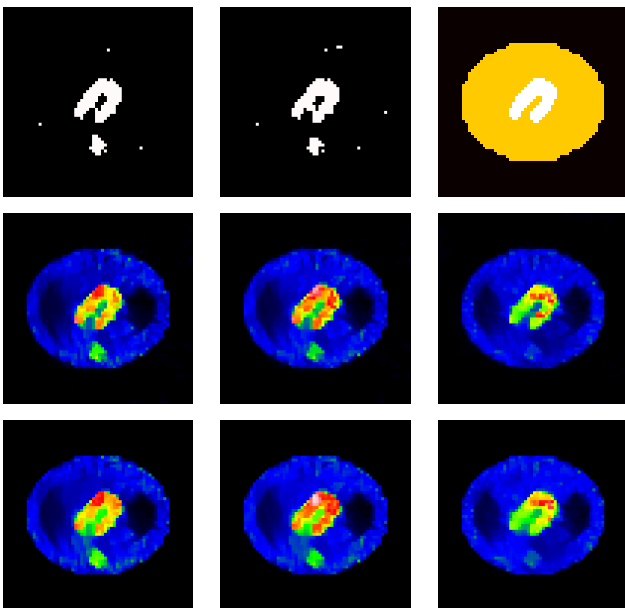


Fig. 7 Simulated Heart Study: Steps on the way to the reconstruction. Line 1 shows detected dynamic zones: Gauss (left), Poisson (middle), obtained by fitting hat functions. Line 1 (right) shows correct answer. Due to strong attenuation, the spinal cord was erroneously interpreted as a dynamic zone. Line 2 shows hat reconstructions: Gauss at times 10, 20, 40. Line 3 same for Poisson.